Instruments and Experimental Techniques, Vol. 46, No. 4, 2003, pp. 521–535. Translated from Pribory i Tekhnika Eksperimenta, No. 4, 2003, pp. 100–115.

GENERAL EXPERIMENTAL TECHNIQUES

Methods of Recording Subtractive X-Ray Projections

A. G. Touryanskii and I. V. Pirshin

Lebedev Institute of Physics, Russian Academy of Sciences, Leninskii pr. 53, Moscow, 119991 Russia

e-mail: tour@mail1.lebedev.ru

Received December 15, 2002

Abstract—Conditions for enhancing image contrast by the digital subtraction of X-ray projections registered at different spectrum distributions in the energy range of 5–25 keV are considered. An experimental scheme for recording digital projections based on a 1300×1030 detecting array with a pixel size of 6.7 μm is described. It is shown that, when an object is irradiated by polychromatic radiation, the use of a Ni filter and a $NiCl_2$ contrast solution provides results that were previously obtained by subtracting images on monochromatic spectral lines near the *K* jump in the absorption of the contrast substance. Schemes for recording color X-ray images in a dynamic mode using semitransparent X-ray monochromators are proposed.

INTRODUCTION

When recording two-dimensional X-ray projections of inhomogeneous objects, the problem of detecting low-contrast elements against the background of a complex image structure usually arises. An efficient method for solving this problem is enhancing the contrast of the object's internal elements using a substance with a linear extinction factor μ that significantly differs from the corresponding parameter of the environment. This technique is widely used in medicine, where contrasting is usually provided with the help of compounds of heavy elements with atomic numbers $Z > 50$: I, Ba, Ta, and Xe [1–4]. In some cases, air or other gases can be pumped into the cavity [1, 2]. When the volume of the object under study or an adjacent region between organs is filled with a gas, the increase in their volumes additionally contributes to the improvement of the contrast.

Combining the methods of contrasting and subtracting images, which were obtained, for example, before and after the introduction of a contrast substance [5], is a way to develop this diagnostic technique. This makes it possible to largely reduce the effect of the superposition of images of various internal organs and to selectively distinguish contrast structures. The selective discrimination of the structural details being studies is especially efficient when narrow spectral bands are used, which are positioned on both sides of the *K* jump in the photoabsorption spectrum of the contrast element [6, 7]. When two detecting systems are used, the projection schemes [6, 7] also allow dynamic difference images to be obtained. The procedure of the dynamic subtraction of images became technically efficient after putting into practice digital methods for data registration, image-field discretization, and describing the field in the form of a matrix. Each element of this matrix characterizes a local value of the radiation flux density transmitted through the object.

However, the methods of recording difference images with the selection of specified spectral bands are not widely practiced. This is due to the necessity of using synchrotron sources whose technical parameters exclude their application in clinical conditions for the time being [8].

This work shows that the methods developed by us of the selection of spectral lines using semitransparent X-ray monochromators (SXMs) [9–12] can be applied to solving the problem of the dynamic visualization of difference X-ray images. The practical capabilities of the difference method will be demonstrated with a projection scheme based on selective filters and a standard X-ray tube, which qualitatively imitates the spectrum transformations obtained using SXMs. In conclusion, we will compare the difference method to the phase contrast method.

SEMITRANSPARENT MONOCHROMATORS

A semitransparent X-ray monochromator is a crystal or an artificial periodic structure [9, 10] satisfying the following requirements: (1) when an SXM is set on the spectral line λ_1 at the Bragg diffraction angle, the condition $T(\lambda_2) \geq 0.5$, where $T(\lambda_2)$ is the transmittance at the spectral line λ_2, should be valid and (2) $\Delta\lambda < |\lambda_2 - \lambda_1| \ll \lambda_1$, where $\Delta\lambda$ is the spectral band of the SXM-reflected radiation.

0020-4412/03/4604-0521$25.00

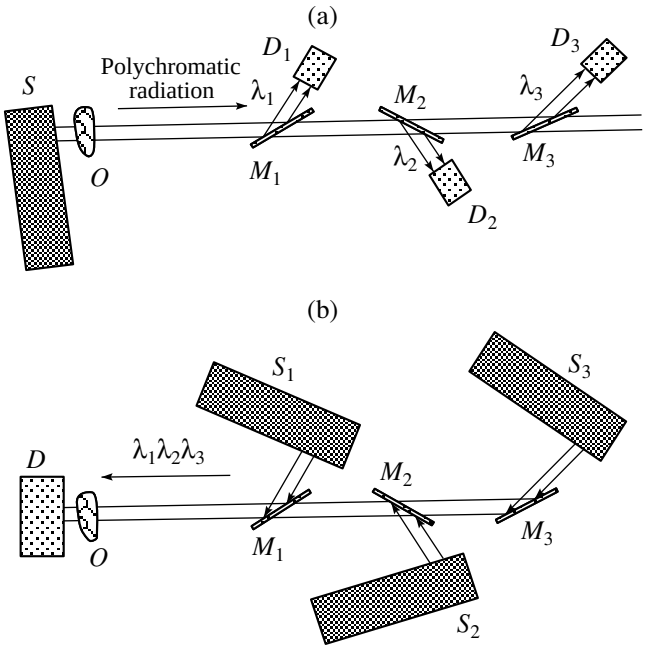

Fig. 1. Diagrams of systems for spectrum conversion using semitransparent monochromators by (a) selecting and (b) mixing spectral lines λ_1, λ_2, and λ_3: (S, S_1–S_3) sources of polychromatic radiation; (D) detecting array; (D_1–D_3) photodetectors; (M_1–M_3) semitransparent monochromators; and (O) object under study.

As was shown in [13], these requirements can also be met with the use of a nontransparent crystal plate or a multilayer structure on a substrate, if the crystal or substrate have through slits oriented in a special manner. From the practical point of view, the SXMs meeting the condition

$$Q(\lambda_1, \lambda_2) = R(\lambda_1) + T(\lambda_2) > 1 \qquad (1)$$

are of greatest interest. Here, $R(\lambda_1)$ is the maximum (peak) monochromator reflection coefficient at the Bragg angle for the line of λ_1.

For an SXM made of pyrolitic graphite 40–60 μm thick, $Q(\lambda_1, \lambda_2)$ = 1.1–1.2 was obtained using the CuK_α(0.154 nm) and CuK_β (0.139 nm) spectral lines [9]. In this case, the half-height angular width, caused by mottling, $\Delta\omega$ of the rocking curves was 0.4°–0.6° at a fixed detector position. A further increase in $Q(\lambda_1, \lambda_2)$ is possible in principle, because, in agreement with the dynamic theory of X-ray diffraction [14, 15], the reflection coefficient R in perfect crystals with a thickness $d \sim$ 10 μm is $R \sim 1$. Then, for $\lambda_2 < 0.1$ nm, $Q \longrightarrow 2$ within narrow spectral and angular ranges, since the absorption in monochromators based on Si and other light elements can be neglected for such a value of d. However, the narrowing of the spectral and angular bands leads to a significant decrease in the light-gathering power of the X-ray optical system, which cannot be justified from a practical viewpoint in most cases.

Satisfying condition (1) for two or more SXMs provides the possibility of selecting specified spectral lines from a polychromatic beam using the scheme shown in Fig. 1a. If the spectrum of a directed polychromatic beam contains spectral lines λ_1, λ_2, and λ_3, then, if the semitransparent monochromators M_1–M_3 are set at the corresponding Bragg angles θ_1, θ_2, and θ_3, these lines are directed to detectors D_1–D_3. The sets of spectral lines with wavelengths λ_1/n, λ_2/n, and λ_3/n (n = 1, 2, 3, …) corresponding to different orders of reflection generally satisfy the Bragg conditions. When the spectral bands of the second or higher orders of reflection represent the bremsstrahlung part of the X-ray tube spectrum, their intensity can be neglected.

If the SXMs are positioned in a row, the intensity of the radiation selected from the primary spectrum by the kth monochromator, which is adjusted to the line λ_k, is

$$I(\lambda_k) = I_0(\lambda_k)R_k(\lambda_k)\prod_{i=1}^{i=k-1} T_i(\lambda_k), \qquad (2)$$

where $I_0(\lambda_k)$ is the intensity of the line λ_k in the forward beam.

SCHEMES FOR RECORDING DIFFERENCE IMAGES

Assume that the detectors D_1–D_3 in the aligned system (Fig. 1a) are replaced by sources of polychromatic radiation S_1–S_3 and the source S is replaced by a detector D. Then, if the spectrum of the sources S_1–S_3 contains spectral lines λ_1, λ_2, and λ_3, after the reflection from the SXMs M_1–M_3 tuned to the corresponding Bragg angles θ_1, θ_2, and θ_3, the radiation containing the aforementioned spectral lines propagates in the direction of D (Fig. 1b).

Such an approach lying in the reversal of X-ray beams can be used for creating a projection device for the dynamic visualization of difference X-ray images and obtaining color X-ray images.

The practical implementation of the device using the scheme shown in Fig. 1b requires that the specified spectral lines be sequentially transmitted through the object and the projections be registered by a two-dimensional photodetector based, for example, on a solid-state detecting matrix. The object is irradiated at a given spectral line by alternately switching the sources S_1–S_3 on and off. The moments that the data-acquisition starts and ends are synchronized by a control computer. If the angular widths of the beams selected by the monochromators M_1–M_3 are the same, then the images in different spectral ranges completely coincide during the registration of projections. The subtraction of the projections obtained at the selected pair of spectral lines is performed after the digital data are transferred to the computer.

In the technically simpler second version, only one X-ray tube operating in a cw mode is used (Fig. 2). Therefore, when using pure-metal anodes, only one pair of the most intense characteristic lines of the K series can be selected: K_α and K_β. The sequential transmission of the specified spectral lines through the object is then accomplished by alternately shifting an absorbing screen *2* set up between the source and monochromators, of which only the monochromator *4* must be semitransparent.

To obtain additional spectral lines, the tube anode can be coated with a thin film of specified chemical composition or made compounded from different materials. If a system of control electrodes, which shifts of the focus position over the anode plane, is built in the tube, the absorbing screen becomes unnecessary.

To optimize the noise level, the irradiation durations Δt_1 and Δt_2 at the spectral lines λ_1 and λ_2 are selected from the condition $\Delta t_2/\Delta t_1 = I^t(\lambda_1)/I^t(\lambda_2)$, where $I^t(\lambda_1)$ and $I^t(\lambda_2)$ are the average radiation intensities at lines λ_1 and λ_2 after the transmission through the object under study. The time of obtaining a complete frame of an image is now limited by the response speed of the photodetector and amounts to 10^{-2}–10^{-1} s for detectors based on CCD arrays with ~10^6 pixels (see below). This limitation is connected with the procedure of sequentially reading the charges of the CCD array and digitizing the data. A further increase in the image-frame readout rate is achieved using detecting matrices based on metal–oxide–semiconductor complementary structures. Their prototypes were manufactured by several companies [16].

When X-ray sources are used, the irradiation time can be made arbitrarily short if the pulse power is sufficiently high to ensure a specified signal-to-noise ratio in the recorded image. The minimum pulse duration obtained experimentally is $t_p \le 1$ ps under excitation by femtosecond lasers and using laser–electron sources [17, 18]. In commercial pulsed X-ray tubes, t_p = 10–100 ns [19]. When pulses from different sources are synchronized, the spectrum switching time can be ~t_p, which is obviously shorter than the time the photodetector takes to read a single frame.

The practical implementation of the schemes considered above requires homogeneous SXMs with a comparatively large area. For example, when using a pyrographite-based SXM, obtaining a beam of a square cross section with an area of 1 cm^2 at the CuK_α line requires a monochromator measuring 1×4 cm^2. SXMs with larger areas can be assembled from several elements. In order to exclude image blurring, the average rotation angle $\langle\Delta\omega\rangle$ of mosaic blocks must satisfy the condition

$$\langle\Delta\omega\rangle l_m \le r_s, \qquad (3)$$

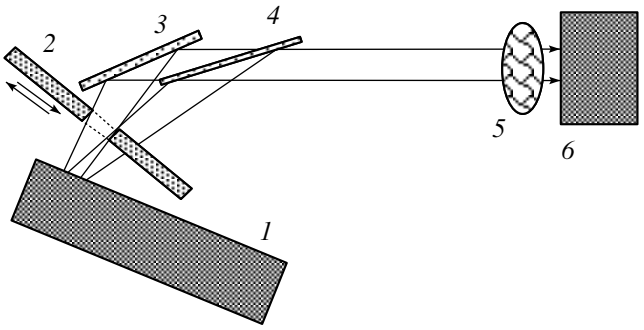

Fig. 2. Diagram of the system for recording difference X-ray images in the dynamic mode with a common source: (*1*) X-ray tube; (*2*) shutter; (*3*) massive monochromator; (*4*) semitransparent monochromator; (*5*) object under study; and (*6*) detecting array.

where r_s is the spatial resolution of the detecting system and l_m is the maximum distance from the object's element to the detecting element of the photodetector.

Pyrolitic graphite monochromators were manufactured in the form of films with areas of 4 and 12 cm^2 (Optigraph, Moscow) for studies of the local distributions $R(x, y)$ and $\Delta\omega(x, y)$. The average film thickness was 46 and 5 μm. The 46-μm-thick film was fixed by its edges in a U-shaped holder, and the other film was placed on an optically polished glass plate. The glass plate was only a mechanical support preventing a pyrographite warping. Therefore, in practice, the condition $T(\lambda) \ge 0.5$ for an SXM can be fulfilled by substituting beryllium for the glass.

The local characteristics were measured by linearly scanning the beam 50 μm in diameter and rocking the sample at a stationary position of the photodetector, in front of which a reception slit 1 mm wide was located. The Cu$K_{\alpha 1}$ spectral line was selected by a Si(111) single crystal.

Figure 3a shows changes in the local value of the reflectivity $R(y, x_0)$ during linear scanning in the direction normal to the diffraction plane for an SXM 46 μm thick (x_0 is a fixed coordinate). The angular dependence $R(\omega)$ was measured at fixed y values marked as A, B, C, and D in Fig. 3a by rocking a sample around the ω axis normal to the diffraction plane. The results of this measurement and numerical processing are presented in Fig. 3b, where I^Σ are the normalized values of the integral sums under curves $R(\omega)$ at positions A, B, C, and D. Figure 3c shows the angular dependences of the radiation intensity $I^R(\omega)$ reflected by the 5-μm-thick film for three arbitrarily chosen areas. The minimum half-width $\Delta\omega$ of its rocking curves decreases to 4.2′ compared to 23.4′ for the 46-μm-thick film. The angular shifts of the peaks of the curves $R(\omega)$ are 2.4′ and 13.9′ for the thin and thick curves, respectively.

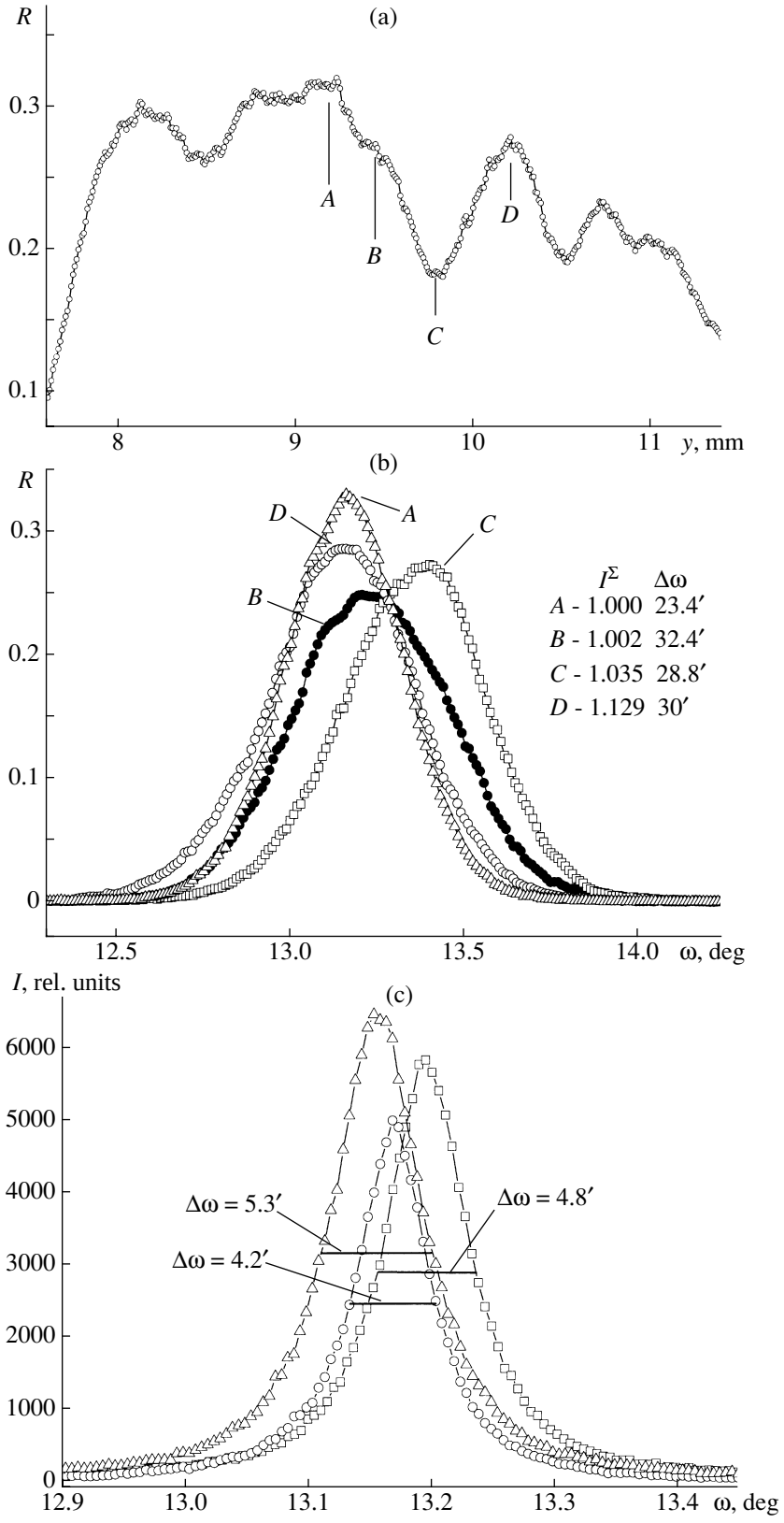

Fig. 3. Characteristics of SXMs of pyrolitic graphite 46 μm thick: (a) local distribution of the reflectivity during linear scanning with a diaphragm 50 μm in diameter; (b) angular dependences of the reflectivity (ω-rocking of a sample) under the local irradiation of regions *A*, *B*, *C*, and *D*; and (c) angular dependences of the reflectivity (ω-rocking of samples) for three parts of a pyrographite film 5 μm thick.

These data show that the local changes in $R(y)$ in Fig. 3a are primarily determined by a shift of the center of gravity of the reflection curves $R(\omega)$, since the dependence $R(y)$ is recorded at a fixed angle $\omega_0 = \theta_B$ is the Bragg diffraction angle for the (0002) graphite reflection at the CuK_α line. At the maximum and minimum R values at points A and C, respectively, in Fig. 3a, the relative value of the difference $I^\Sigma(C) - I^\Sigma(A)$ is 3.5%. This indicates that the main cause of local R changes is the warping of the pyrographite film during the manufacture of the SXM. As the film thickness grows, the turns of mosaic blocks increases in the bulk of the film. This means that homogeneous SXMs, which are necessary for obtaining images, can be obtained by transferring pyrographite onto a thin optically polished substrate made of a weakly absorbing material, such as beryllium. The reflectivity can be increased by using a structure containing several reflecting layers.

An increase in the X-ray flux density, which is necessary for shortening the time required to obtain an image exposure, can be attained with the help of polycapillary half-lenses placed between the radiation source and the SXM [20, 21].

Hence, the data presented allow us to conclude that there is currently a technological base for designing practical schemes for visualizing X-ray images based on SXMs. The schemes depicted in Figs. 1b and 2 allow us (a) to combine the images recorded in different bands of the X-ray spectrum so that they coincide and (b) to switch the spectrum in a time much shorter than the characteristic times of periodic processes in biological objects (~1 s for cardiac contractions and 2–4 s for an inhalation–exhalation cycle). This suffices for solving the formulated problem of recording difference dynamic images.

Note that the procedure of recording projections using the schemes in Fig. 1b is formally equivalent to the obtainment of color images in the optical band. Therefore, the color coding algorithms considered, for example, in [5] can be used for constructing color X-ray images.

PROJECTION SCHEME WITH REPLACEABLE FILTERS

The scheme for obtaining difference images used in this study is shown in Fig. 4. The radiation source was a 1-kW X-ray tube with a copper anode. Radiation with an energy <5 keV was filtered due to its attenuation in air. The spectrum of X rays incident on the sample was modified by using a Ni (15 μm), Al (40 μm), or Cu (20 μm) foil and also by changing the high voltage at the X-ray tube in steps between 11 and 25 kV. Introducing filters provided an attenuation of the hard portion of the spectrum with an energy exceeding the K edge of the photoabsorption jump.

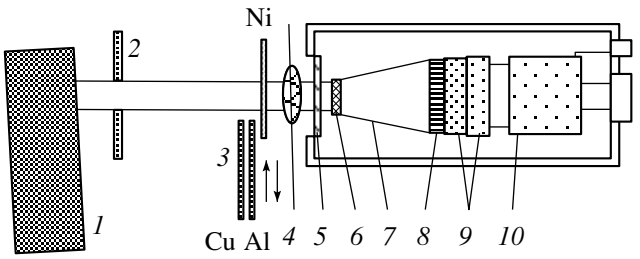

Fig. 4. Experimental system for recording X-ray projections based on selective filters and a detecting array: (*1*) X-ray source; (*2*) collimator; (*3*) set of filters; (*4*) object; (*5*) Be window; (*6*) scintillator; (*7*) phocon; (*8*) CCD array; (*9*) Peltier elements; and (*10*) electronic unit.

The two-dimensional (2D) distribution of the radiation flux density was registered by an FDI detector (Photonic Science, Great Britain). The basic detector elements are a CCD array with 1300 × 1030 photosensitive cells, a fiber-optic cable of variable cross section, and a scintillator layer deposited on the cable end. A Gd oxysulfide polycrystal with a surface density of 10–15 mg/cm^2 is used as the scintillator. A two-stage cooling system based on Peltier elements reduces the temperature of the array by ≥40°C compared to the environment. Recording 16 exposures/s in a dynamic range of 10 bit is ensured at an interrogation rate f = 20 MHz. All of the results presented in this work were obtained at f = 10 MHz. In this case, a dynamic range of ~12 bits is attained. In units of the elementary charge e^-, the dynamic range amounts to 22 ke^-. The average zero signal level is shifted by ≥5 bits.

The possibility of a stepwise (100 steps) change in the gain of the primary signal of the CCD array in the range of 1 : 6 is provided. The setting of the conditions for data acquisition and the processing of 12-bit images were executed using the PhotoLight software package. The diameter of the detector entrance window is 19 mm, and the effective working area of the detector is a rectangle with dimensions of 8.7 × 6.9 mm^2. The 0.25-mm-thick protective membrane is made of polished Be. The image element (pixel) on the detector entrance window has dimensions of 8.7/1300 = 6.9/1030 = 6.7 μm. Sequences containing 1300 and 1030 pixels are considered rows and columns, respectively. The characteristics of the detector obtained experimentally are presented below.

TESTS OF THE SYSTEM

Conversion Relation

The relation between the flux of X-ray quanta P incident on the detector entrance window and its valid output signal S is of practical interest. The signal S is expressed in quantization units of the analog-to-digital converter (ADC) after the CCD array signals are digitized. This relation can be expressed through a dimen-

Table

Exposure no.	Parameter			
	average background value $\langle S_b \rangle$	RMS deviation of the background signal σ_b	background signal	
			s_{min}	s_{max}
With cooling, $N = 10^5$ pixels, $T = 20$ s				
1	33.030	1.280	27	54
2	33.023	1.272	28	49
3	33.024	1.272	28	47
4	33.029	1.272	28	49
5	33.019	1.277	28	47
6	33.015	1.281	28	47
7	33.026	1.271	28	49
8	33.021	1.275	27	47
9	33.018	1.275	28	48
10	33.009	1.2580	28	51
With cooling, $N = 10^5$ pixels, $T = 100$ s				
11	33.1	2.1	26	387
12	32.8	1.4	27	93
13	32.8	1.4	27	81
14	33.5	2.0	28	453
Without cooling, $N = 10^5$ pixels, $T = 100$ s				
15	87.1	22.5	65	2914
16	85.1	12.6	65	1360
17	85.2	12.2	66	1077
18	89.9	23.1	69	2870

sional coefficient, which is a function of the radiation energy:

$$P = SK(E) = K(E)[\Sigma\Sigma S_{ij} - \Sigma\Sigma s_{ij}], \quad (4)$$

where S_{ij} and s_{ij} are the signals from image elements of the CCD array registered with the X-ray source switched on and off; i and j are the numbers of columns and rows of the detecting array, respectively.

The summation is performed over the rectangle bounded by a contour, within which the irradiated zone lies on the entrance window of the detector.

In order to determine $K(E)$ at the standard Cu$K_{\alpha 1}$ line (E = 8.050 keV), a БДС-6 scintillation detector with known detection efficiency was used. The X-ray beam was monochromatized using a Si(111) crystal. The monochromatic beam was sequentially directed to the scintillation and studied detectors through mutually perpendicular slits 0.5 and 1 mm wide. The signal recording time was 100 s.

When the gain step number was set at 5 (see above), the measured value of $K(E)$ was 2.9 X-ray quanta per ADC quantization level. Taking into account the aforementioned parameters of the detecting array, to obtain an image in t = 1 s on the working detector area with an average signal level S = 800, the flux of quanta transmitted through the object must be equal to $P_t \approx 3.9 \times 10^6$ $S = 3.1 \times 10^9$ quanta/s. Note that, in practice, the possibility of reducing P_t by increasing the time is restricted by the value 3×10^2–10^3 s, since a dark signal rapidly rises at certain pixels of the array.

Characteristics of Dark Signals

The table lists the main characteristics of dark detector signals. The data of exposures 1–10 were statistically processed over the rectangular field at the center of the CCD array. The signal storage time was T = 20 s. The selected area contained $N = 10^5$ pixels, which was 7.5% of the total detector area. Rows 1–9 present the results of successive measurements performed at intervals of ~1 min. Row 10 corresponds to the measurements performed 1 h later under identical conditions for data acquisition.

Rows 11–18 list the characteristics of dark signals of the detecting array obtained with and without cooling. The signal storage time is T = 100 s. Four areas containing 10^5 pixels were processed: the first one is at the center of the dark-image field (rows 11 and 15), and the others lie at its corners (rows 12–14 and 16–18).

As follows from the tabulated data (rows 1–10), the basic characteristics of the dark signals of the CCD array remain virtually constant during the measurement period. When the cooling is switched off, the average level of the dark signal $\langle S_b \rangle$ and σ_b increase by factors of 2.6 and *10*, respectively. The values of local surges s_{max} substantially depend on the position of the analyzed area of the array field.

The elements of the CCD array can be conventionally divided into two groups with low and high dark currents. This is illustrated by the distribution s_{ij} over a fragment of an array row (Fig. 5) obtained at T = 20 s. Dark-signal surges on two pixels on the left side of the plot (curve *1*) are caused by the presence of channels for the flow of charge into the potential wells of the corresponding photosensitive elements of the CCD array. The procedure of the numerical subtraction of dark signals obtained in the same row in the next s_{ij} measurement for the same storage time ensures a multiple reduction of surges (curve *2*).

The procedure of subtracting two sequential random noise distributions should increase σ by a factor of $\sqrt{2}$ [22]. In reality, σ rises by a smaller value in the region without surges. This is due to the fact that s_{ij} values contain systematic Δ_{ij} and random δ_{ij} components, and the difference of the systematic deviations tends to zero. The σ values calculated over all of the experimental points (N = 400) and for the right part of the distribution without sharp surges (N = 200) are shown in Fig. 5.

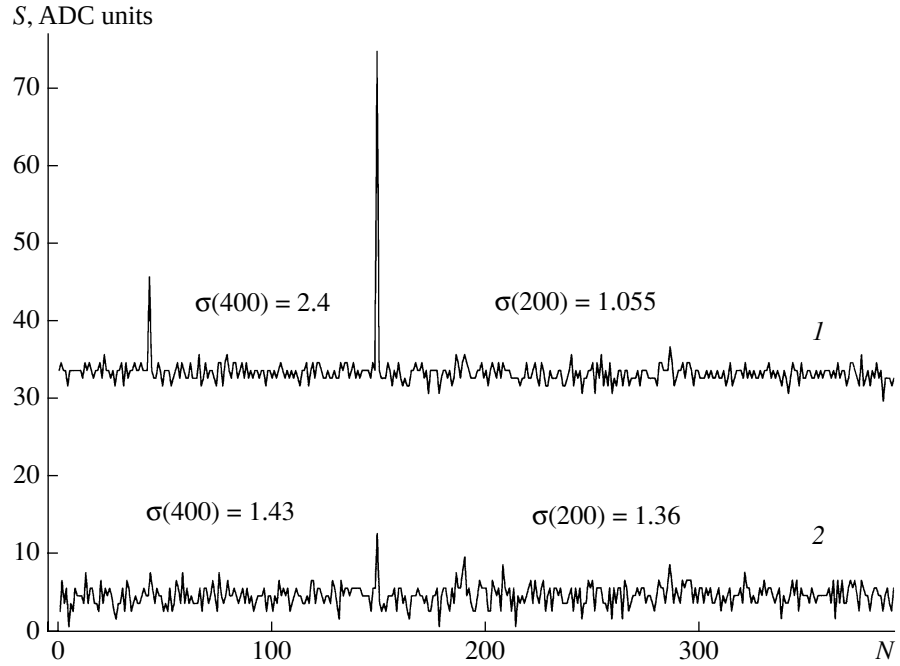

Fig. 5. Distribution of the levels of dark signals over a fragment of a row of the detecting array; the signal storage time is T =20 s: (*1*) the initial signal and (*2*) the difference dark signal at sequential exposures at intervals of 1 min.

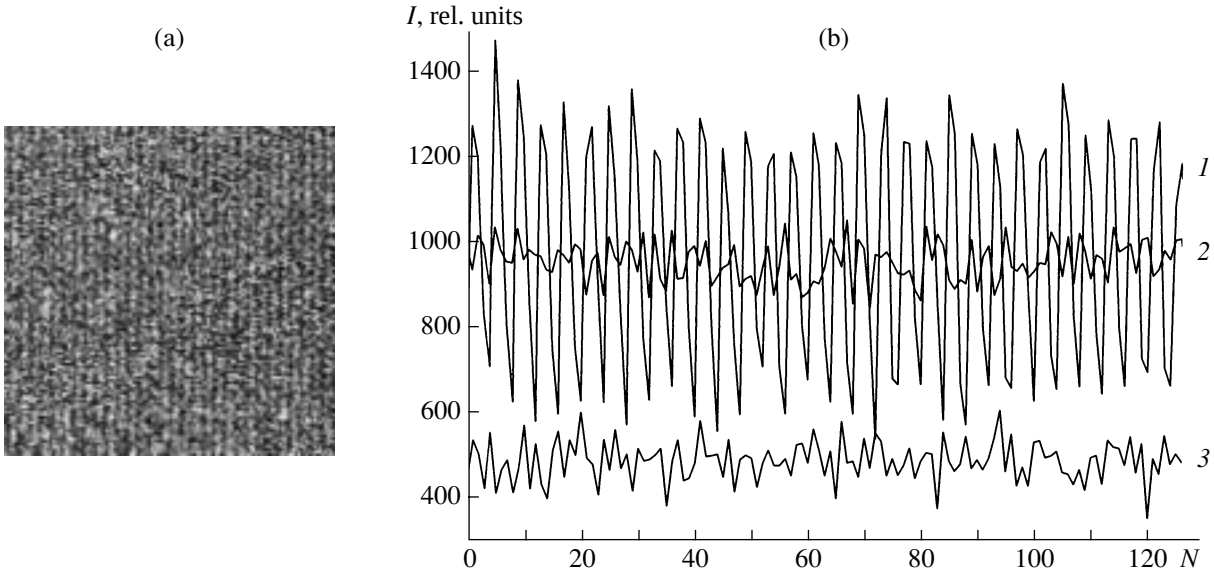

Fig. 6. (a) Dark image of the central zone of the detecting array (N = 250 × 250 pixels and T = 60 s); (b) distributions of levels of the total dark signals from the central zone of the detecting array (T = 60 s): (*1*) summing over the columns; (*2*) summing over the rows; and (*3*) difference of the sums over the columns for two successive measurements at T = 60 s.

Periodic Oscillations of Dark Signals

When weak one-dimensional or quasi-one-dimensional distributions of the X-ray flux density are measured, the signal must be integrated over the rows or columns of the detecting array. In this case, one should know whether this procedure can lead to the appearance of its own systematic signal generated by the CCD-array readout device. Figure 6a presents a dark image of the central rectangular zone containing 250 × 250 pixels and obtained for a storage time of 20 s. Figure 6b shows the results of summing the dark signals over the columns (curve *1*) and rows (curve *2*) versus the numbers of the corresponding columns and rows for a part of this zone. These data show that clearly pronounced oscillations of the dark-field level with a

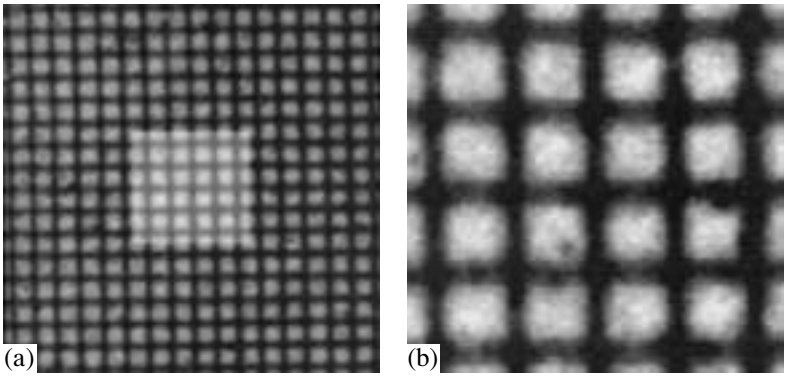

Fig. 7. Images of the test object in the form of a Ni–Cr grid with a pitch of 100 μm: (a) field of 3 × 4 mm and (b) field of 350 × 350 μm.

period of 4 pixels and a total amplitude of ≈250 ADC units or 1 ADC unit per pixel are observed for the summation over the columns. When the difference of two sequential dark images obtained during equal time intervals is taken, periodical oscillations disappear (Fig. 6b, curve *3*). However, this effect is not observed in some tests, which is evidently associated with a random shift of the phase of a spatial harmonic on the image field.

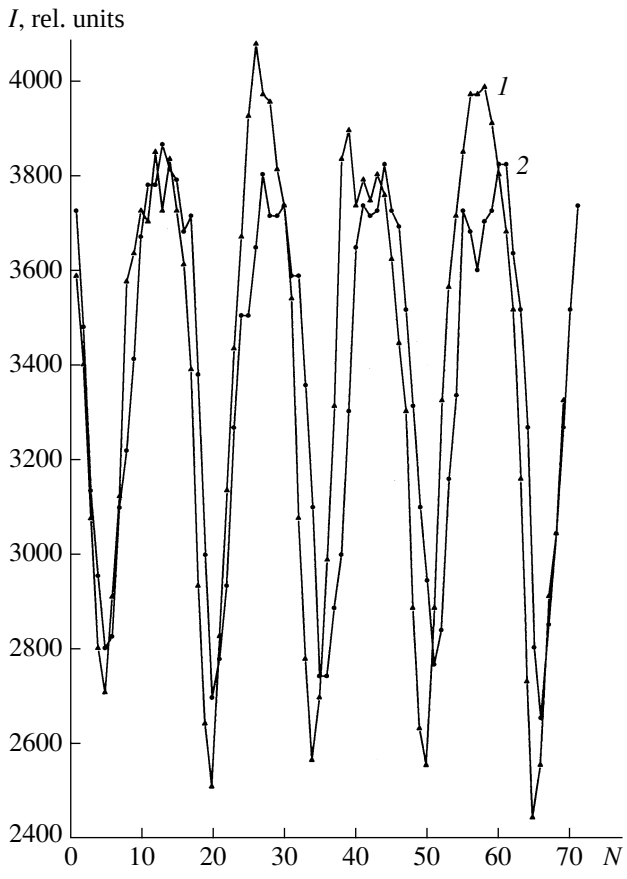

Fig. 8. Modulation of the signal intensity along the (curve *1*) row and (curve *2*) column of the detecting array on a fragment of the image of the grid (Fig. 7b).

Effect of the Size of the Source Focus

A scheme with a point X-ray focus is an optimal one for recording projection images. In practice, the projection of the tube focus onto the image plane has finite dimensions that are usually much larger than the spatial resolution of the X-ray detector. This is dictated by the requirements as to the source power and the generated flux density. Let us consider the possibility of obtaining projections in the system with a linear focus (Fig. 4). If the geometrical parameters are known, such an orientation of the focus allows us to estimate the distance between the detector entrance window and the scintillator layer at the end of the phocon. To solve this problem, it is necessary to minimize the distance between the X-ray-sensitive layer and the detector entrance window and to place the test object directly on this window.

According to our technical requirement specified for the manufacturer of the detector, the distance d between the Be window and the Gd oxysulfide layer must be 0.5–1.0 mm. The sizes of the projection of the focus of the X-ray tube used in experiments were $F_1 = 0.04$ mm and $F_2 = 8$ mm in the horizontal and vertical planes, respectively. The image of a point object, which is placed on the detector entrance window, in the plane coinciding with the X-ray-sensitive layer represents a projection of the focus reduced by a factor of $L/(d + t)$, where t is the thickness of the Be layer and L is the distance from the focus to the detector window. If $d = 0.75$ mm, then, for $L = 580$ mm and thickness $t = 0.25$ mm, the image dimensions are $f_1 = 0.069$ μm and $f_2 = 14$ μm. The value of f_2 is approximately equal to the spatial resolution of the array. According to the measured intensity difference at the edge of the absorbing screen, this resolution is equal to two pixels of the array (13.4 μm). Therefore, despite an obvious astigmatism inherent in the projection scheme with a linear focus, it can be expected that, with the given experimental geometry, no significant image distortions will be observed for $d \le 0.75$ mm.

This is confirmed by the image of a Ni–Cr wire grid with a pitch of 100 μm positioned at the detector entrance window (Fig. 7a). A more detailed graphical comparison of the intensity modulations along an arbitrarily chosen row and column in a fragment of the grid image (Fig. 7b) shows a slight decrease in the signal amplitude along the column caused by the shape of the focus (Fig. 8).

As was noted above, the beam divergence in the diffraction plane can be caused by the turn of crystal SXM blocks. Therefore, if $\Delta\omega < (d + t)/L \approx 1.7$ mrad (5.8'), replacing the selective filters by SXMs will not impair the spatial resolution in the exposure geometry considered.

CONTRAST OF THE PROJECTION DIFFERENCE

In order to explain the features of the perception of the contrast of the image obtained as the difference of two projections, let us emphasize the chief differences between the images recorded in the analog and digital forms and some features of perceiving images in the visible range. Analyzing the contrast, we assume that the relative statistical fluctuations over the image element selected can be neglected compared to the relative change in the signal level quantized in the form of brightness gradations.

As a rule, the contrast of an individual detail C_d of an image and the contrast over the entire image field C are analyzed [23–27]. When analog methods for recording the primary radiation image are used, the following relations are most frequently used to numerically characterize C_d and C:

$$C_d = |\Delta I|/I, \tag{5}$$

$$C = (I_{\max} - I_{\min})/I_{\max}, \tag{6}$$

where ΔI is a small increment of the analog signal of the photodetector created by this detail with respect to the level of the background signal I surrounding the detail.

If $I \propto L$, where L is, for example, the screen glow brightness or the film blackening density, relations (5) and (6) also characterize the optical image of the illuminated object. In practice, when displaying the primary radiation image on a monitor screen, it is necessary to take into account the Weber–Fechner law [28] and perform a nonlinear conversion of the radiation signal. Therefore, the radiation and optical images usually have different contrast characteristics. As a measure of the quality of a radiation image, relation (6) becomes meaningless during digital recording. In fact, since, before displaying a digital image on a screen, it is possible to determine the $I_{\min}$ value using a program and subtract it from the elements of the data matrix, according to (6), any digital image after this procedure can formally have the maximum contrast value $C = 1$.

Under favorable visualization conditions (the image brightness is ~100 cd/m^2 and the angular size of the detail is no less than 0.3°), the minimum visually discerned contrast value is $C_{\min} \approx 0.02$ [25]. The range of the brightness ratio within which the eye can almost uniformly distinguish the contrast gradations produced by image details does not exceed $L_{\max}/L_{\min} = 35$ [29]. According to the Weber–Fechner law, we have the following estimate of the number contrast gradations G_c within this range:

$$G_c = \frac{(\ln L_{\max} - \ln L_{\min})}{\ln(1 + C_{\min})} \approx 180. \tag{7}$$

Hence, for discretely varying black-and-white gradations of the brightness L, it is sufficient to introduce an 8-bit brightness scale providing 256 gradations. It is precisely this scale on which modern graphics editors operating with black-and-white images are based [30]. Scales with wider ranges, such as 12 or 16 bits, are actually used for storing and numerically processing the data array.

In practice, due to the presence of external lighting, the impossibility of a lengthy eye adaptation, an angular dependence of the reflectivity, and other factors, the actually distinguishable range of gradations G_p is no larger than 6–7 bits. Therefore, in order to visually represent any projection containing digital data in the range of quantization levels of $G_e > G_p$, the projection must be transformed by dividing the data array elements by the ratio G_e/G_p. This leads to a loss of data. An alternative approach is to view the image in parts in a window containing the gradation range $(G_i, G_i + G_p)$, where G_i is the lower signal level selected by the observer.

During the digital image recording, the range of measured signal levels is usually much larger than the range of gradations perceived by the eye. For example, in computational tomography, the range of registered gradations of the linear extinction factor in the form of Hownsfield units usually amounts to at least 10 bit, and the technically ensured range is >12 bit [31]. For this reason, the image is represented within a certain window of gradations selected automatically or by an operator. In this case, the image-field areas lying outside of the selected visualization window are represented by a black or white field.

Thus, as applied to a digital image, it is expedient to speak about an optimal contrast at which the number of obtained contrast gradations correspond to the number of visually perceived signal gradations over the entire image field. In this case, the main details of the object's internal structure must be preserved and the data array obtained must be suitable for calculating the parameters of the illuminated object.

When we change to the difference image obtained by subtracting the data array recorded at energies E_1 and E_2, expression (5) for the detail contrast is transformed and takes the form

$$C_d^s = |\Delta I_1 - \Delta I_2|/|I_1 - I_2|. \tag{8}$$

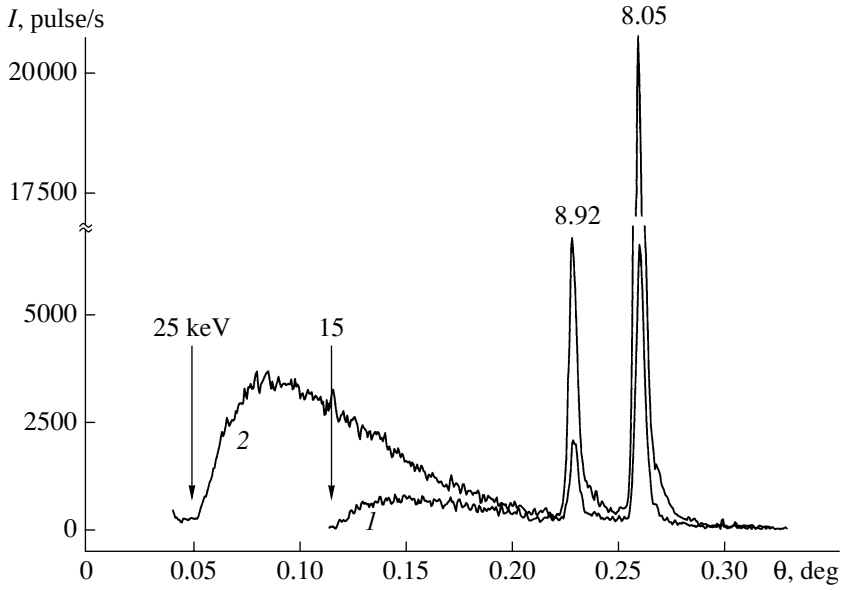

Fig. 9. Angular spectrum of an X-ray tube with a Cu anode at a voltage across the tube of (curve *1*) 15 kV and (curve *2*) 25 kV; the average angle of radiation emission with respect to the anode plane is 5.5°.

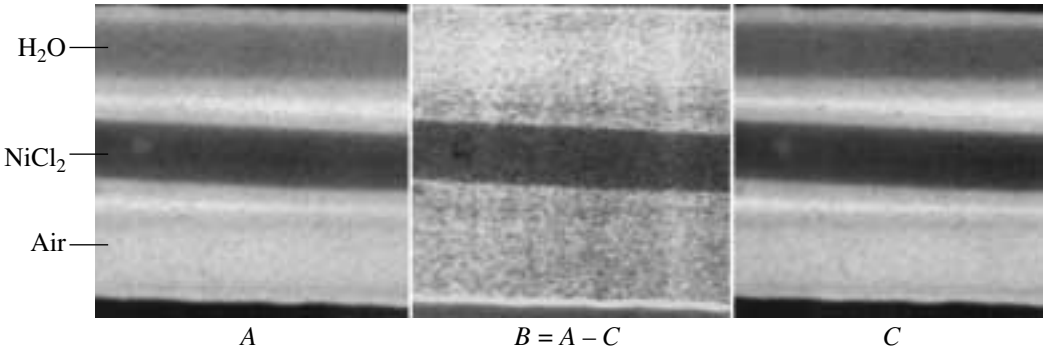

Fig. 10. Triptych of projections of a test object in the form of polyethylene tubes filled with water, a 15% $NiCl_2$ solution, and air: (*A*) 15 kV, 5 mA, and 15 s; and (*C*) 15 kV, 15 mA, 13 s, and a Ni filter.

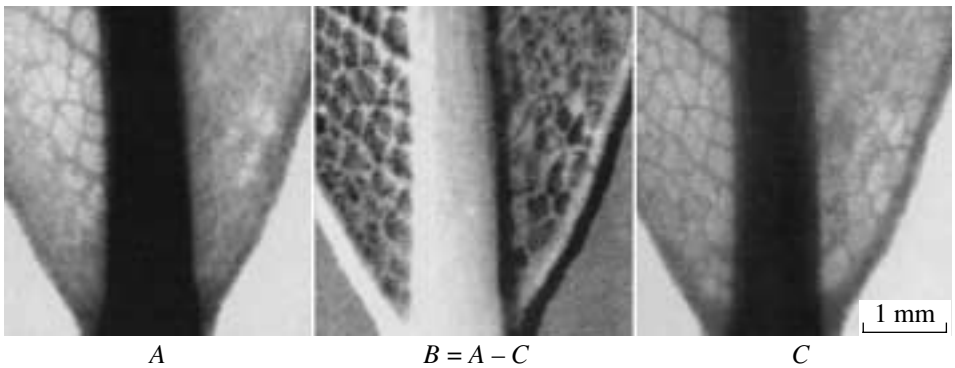

Fig. 11. Triptych of projections of a leaf of *Laurus nobilis*: (*A*) 15 kV, 15 mA, 10 s, and a Ni filter; and (*C*) 25 kV, 15 mA, and 6 s.

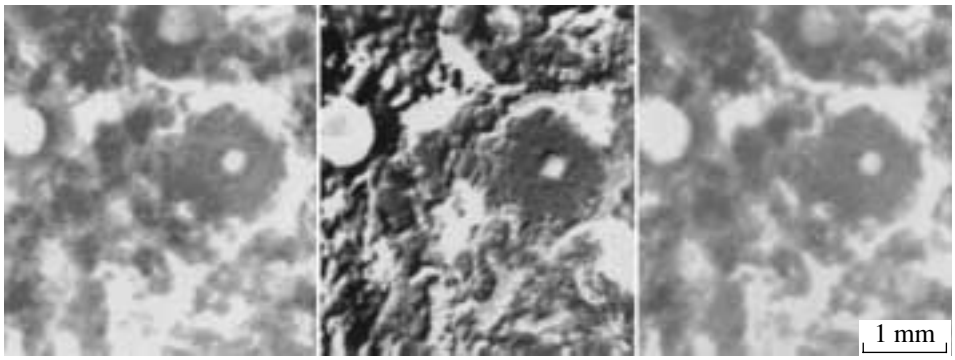

Fig. 12. Triptych of projections of a cut of a mandarine peel: (*A*) 15 kV, 15 mA, 70 s, and a Ni filter; and (*C*) 20 kV, 5 mA, and 30 s.

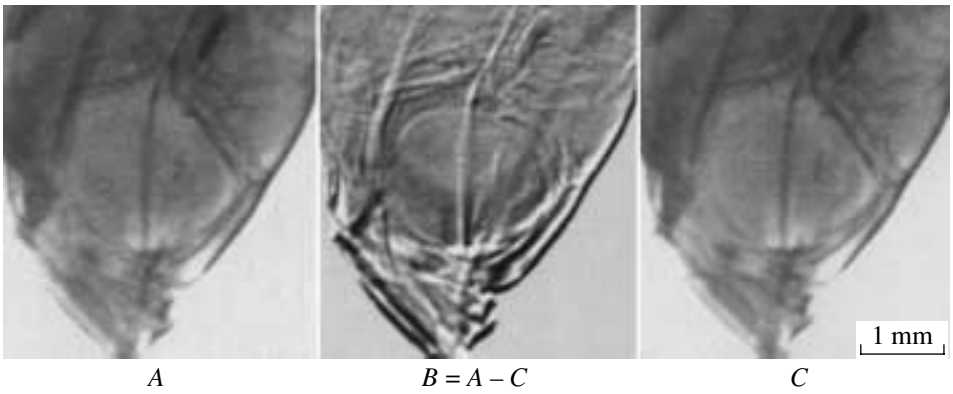

Fig. 13. Triptych of projections of a *Tanychtys albonubes* aquarium fish: (*A*) 15 kV, 15 mA, 11 s, and a Ni filter; and (*C*) 20 kV, 15 mA, and 6 s.

Let us now assume for definitiveness that the element examined is a disk with a thickness Δx whose axis is parallel to the incident beam. This element lies in a layer of the substance whose composition and density differs from the element substance. The relative change in the signal produced by the element is small compared to the signal recorded upon passage of X rays through the object: $\Delta I_1 \ll I_1$ and $\Delta I_2 \ll I_2$. Let us assume that $E_1 < E_2$ and $I_1 \neq I_2$. Expanding the exponential function, which describes the extinction of monochromatic radiation in the substance, into a power series and rejecting the terms with a power exceeding one, after transformations, we obtain the following expression for the difference contrast:

$$C_d^s(E_1, E_2) = \frac{\Delta x|(\mu_1 - \gamma\mu_2)|}{|1-\gamma|}, \qquad (9)$$

where μ_1 and μ_2 are the linear extinction factors for radiation with the energies E_1 and E_2, and $\gamma = I_2/I_1$.

The subtraction procedure is of practical importance, if it enhances the contrast, i.e., the following conditions are met:

$$C_d(E_1) < C_d^s(E_1, E_2) \text{ and } C_d(E_2) < C_d^s(E_1, E_2).$$

Using expressions (5) and (9), these conditions can be written in the form

$$\begin{cases} \mu_1 < \dfrac{|(\mu_1 - \gamma\mu_2)|}{|1-\gamma|} \\ \mu_2 < \dfrac{|(\mu_1 - \gamma\mu_2)|}{|1-\gamma|}. \end{cases} \qquad (10)$$

Let us analyze expressions (10). At $E_1 = E_2$ ($I_2 \neq I_1$), the linear extinction factors are equal to each other, and system (10) results in identical equalities. This means that linear combinations of the data measured at an unaltered spectral composition of radiation do not provide an increase in the difference contrast.

At energies $E > E_{K_m}$, the energy dependence of the mass radiation extinction factor in a material is satisfactorily described by the function $\mu(E) = (E_0/E)^3\mu(E_0)$ [19], where E_{K_m} is the maximum energy of the edge of the K jump of photoabsorption for the chemical elements incorporated in the object[1] and E_0 is an arbitrarily chosen reference radiation energy value ($E_0 >$

[1] For heavy elements, it is also necessary to consider the energies of L jumps of photoabsorption.

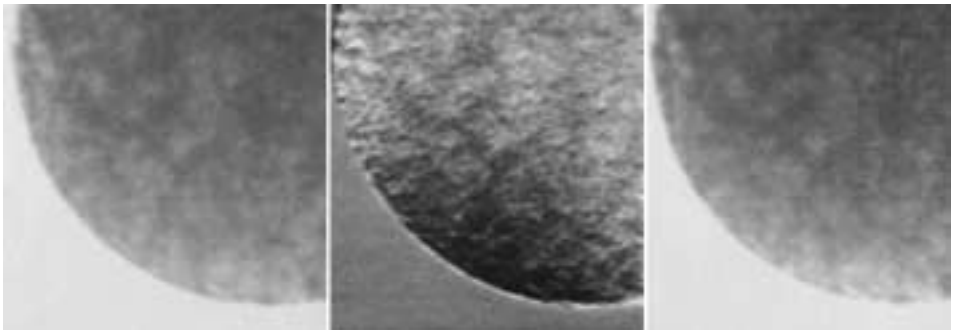

A *B = A – C* *C*

Fig. 14. Triptych of projections of a tablet of orthophene: (*A*) 15 kV, 15 mA, and 10 s; and (*C*) 15 kV, 15 mA, and 120 s, and a Ni filter.

E_{K_m}). Since $E_2 > E_1$, $\mu_1 > \mu_2$. Therefore, to enhance the contrast, it is enough to fulfill the first inequality in (10), which, after the substitution of the appropriate expressions for $\mu(E)$, is transformed into the form

$$1 < \frac{\left|(1-\gamma(E_1/E_2)^3)\right|}{|1-\gamma|}. \qquad (11)$$

It is obvious that, for $\gamma < 1$, condition (11) is always met if $E_2 > E_1$. Thus, the contrast of the difference image can be enhanced with an appropriate selection of the radiation parameters without using contrast substances.

If the energies E_1 and E_2 lie on opposite sides of E_K ($E_1 < E_K < E_2$), where E_K is the energy of the *K* edge of photoabsorption in the object's element, then, as is shown below, the μ_2 value increases jumpwise. Therefore, an abrupt contrast increase must be observed at $|1-\gamma| \ll 1$.

The possibilities of obtaining difference images using special contrast substances and varying the spectrum will be demonstrated for several biological objects.

CONTRASTING OF OBJECTS

The average photon energies of the doublet of the CuK_α spectral line and the CuK_β line and the energy E_K(Ni) of the *K* edge of photoabsorption in Ni are 8.041, 8.905, and 8.332 keV, respectively [32]. Thus, the condition $E_K(\text{Ni}) < E(\text{Cu}K_\beta)$ is satisfied for the CuK_β line, and the ionization of the *K* shell makes the chief contribution to the photoabsorption cross section for X-ray quanta [33]. Therefore, when changing from the Cu-K_α to CuK_β line, the mass extinction factor μ_m in Ni increases jumpwise from 48.5 to 282 cm^2/g [32]. This means that, if spectral lines of Cu and substances containing Ni are used, we can expect an increased contrast of the Ni-containing object's elements in difference images. When polychromatic radiation is modified with selective filters in the system shown in Fig. 4, the effect of the photoabsorption jump in Ni is retained.

Figure 9 shows the tube spectrum after its conversion into an angular intensity distribution using a diamond prism [34]. This spectrum can be conventionally divided into hard $\{E > E_K(\text{Ni})\}$ and soft $\{E < E_K(\text{Ni})\}$ parts. Therefore, the sequential recording of projections with and without a filter is qualitatively equivalent to simultaneous measurements at two and one spectral lines. If radiation fluxes in the soft and hard spectral regions are of the same order of magnitude, then an enhanced contrast of the Ni-containing element and the leveling of signals from the neighboring noncontrast object's parts can be expected in difference images. This is confirmed by the comparison of ordinary projection images of a test object in the form of plastic tubes 1 mm in diameter filled (from the top to the bottom) with water, a 15% solution of $NiCl_2$, and air (Figs. 10 *A*, 10 *C*) and the difference image (Fig. 10 *B*). In the difference image, the contrast of the volume with the Ni solution increases and the image of the other tubes, which are clearly seen in the upper and bottom parts of Figs. 10 *A* and 10 *C*, virtually disappears.

The object's elements can be contrasted by selectively depositing the $NiCl_2$ salt on the surface or diffusing through the object's surface. Figure 11 shows a projection triptych of a leaf from a Grecian laureal (Laurus nobilis [ital]) after its treatment in a 20% $NiCl_2$ solution. This procedure included boiling for 10 min and subsequent holding for 7 days at room temperature. As the comparison shows, the difference image $B = A - C$ has a pronounced stereoeffect.

A similar result was obtained on a cut of a mandarine peel ~1 mm thick (Fig. 12). The cut was kept in the 20% $NiCl_2$ solution for 7 days at room temperature. Due to the stereo effect, the difference image authentically reproduces the morphology of the object's surface. In particular, pores are easily identified in Fig. 12 *B*. The boundaries of structures of the difference image are sharp and contain many small details without a combination of pairs of black and white spots, which is characteristic of a linear displacement of the object. This points to an absorption origin of the stereo image.

We also contrasted fragments of biological tissues of rats by injecting an aqueous solution of $NiCl_2$ with a concentration of 10–30% into the vascular system. The interval between the preparation of the rat and the X-ray investigation was ~10 h. As follows from the experiments, the $NiCl_2$ solution interacts with the tissue of vessels and diffuses through their walls into the surrounding volume. Therefore, this time interval between the preparation and measurement did not allow us to attain a pronounced selective contrast.

CONTRAST ENHANCEMENT AS A RESULT OF SPECTRUM VARIATION

Earlier, we analyzed the conditions for enhancing the contrast in difference images without using a contrast substance by selecting an energy of spectral bands. Figures 13 and 14 show projection triptychs of an aquarium fish *Tanychthys albonudes* and a tablet of orthophene, respectively, obtained only by varying the spectrum of radiation incident on the sample. These images confirm the possibility of observing a similar effect also in polychromatic radiation. A slight blurring of the difference image in the bottom part of Fig. 13 *B* is caused by the shrinkage of the object dried out in air.

COMPARISON WITH PHASE CONTRAST METHOD

The images presented above were obtained using wide polychromatic-radiation bands in the range of 5–25 keV. For monochromatic radiation in the same energy range, images of biological objects were obtained using the refraction or phase contrast method [35–41]. The refractive index of biological tissue in the hard X-ray range is usually written in the form $n \approx 1 - \delta$, where δ is the decrement of the refractive index. If $E > 10$ keV, then $\delta(E) \leq 10^{-6}$. If we have an extended plane interface, X rays with an energy E are deflected near its edge by an angle

$$\Delta\theta(E) = \sqrt{2/\delta_d(E) - \delta'_B(E)}, \qquad (12)$$

with respect to the initial direction. Here, $\delta_d(E)$ and $\delta_B(E)$ are the refractive indices of the detail and the environment [34].

At the interface where the X rays enter a less optically dense medium, a specular reflection with a maximum deflection angle $2\theta_c(E)$, where $\theta_c(E)$ is the critical angle of total external reflection, can be observed. Then, values of the angles $\Delta\theta(E) \sim 1$ mrad can be formally obtained for the case considered. This is easily registered in experiments. However, interfaces in biological tissues have a continuously changing radius of curvature and, due to the cellular structure of tissues, the latter are not smooth, making it impossible to observe an appreciable contribution of the effects considered to the X-ray scattering pattern.

It is known that biological tissues contain structures in the form of cylinders (blood capillaries, bronchioles, etc.). Such objects can be regarded as cylindrical lenses with a focal length $R/2\delta(E)$, where R is the radius of the cylinder [42]. Therefore, to observe the phase contrast, it is necessary to register deflections of the wave front in monochromatic radiation by angles $\Delta\theta \approx 2\delta(E)$ (i.e., ~1 μrad). In experiments with an X-ray interferometer [36, 37], a phase incursion $\mathbf{k}\Delta nl$ in the direction of the primary wave can be registered. Here, $\mathbf{k}$ is the wave vector, Δn is the difference between the refractive indices of the object's detail and the surrounding substance, and l is the size of the detail. However, due to stringent requirements as to the thermal stabilization and limitations due to its overall dimensions, the interferometer can be used only in the laboratory for objects with a size of ~1 cm. In experiments with a phase contrast, at least two monochromators are usually used. They are positioned in front of and behind the object under study along the X-ray path [38–41]. As was shown in [35], the crystal–analyzer can be replaced by a multilayer structure with a narrow resonance-absorption band. At diffraction angles $\theta_B \sim 10°$, a deflection of radiation by an angle $\Delta\varphi$ in the plane normal to the diffraction plane results in a change in the diffraction angle by a value $\sim(\Delta\varphi)^2$.

Since the condition $\Delta\theta \geq (\Delta\varphi)^2$ must be satisfied, the quantity $\Delta\Omega \approx \Delta\theta\sqrt{\Delta\theta} \approx 10^{-9}$ sr can be taken as the maximum acceptable solid angle within which the radiation incident on a point detail of the illuminated object may propagate. It was shown above that the satisfactory quality of projection images of a test object in the form of a grid was obtained at an angular beam divergence $\Delta\theta = 1.7$ mrad in the vertical plane. A similar angular divergence is also acceptable in the horizontal plane. Therefore, in difference measurements under the aforementioned conditions, we obtain the corresponding value $\Delta\Omega \approx 3 \times 10^{-6}$ sr. This implies that, first, the phase-contrast images can be obtained in a time suitable from the viewpoint of practical diagnostics only using high-power directed X-ray sources. Second, since $\Delta\theta \ll \Delta\varphi$ in most cases, small angular deflections of the X-ray beam in a direction perpendicular to the diffraction plane are not detected in schemes for the observation of the phase contrast and, hence, have no effect on the contrast of details of the image.

CONCLUSIONS

The results presented allow us to make the following conclusions.

(1) Under the experimental conditions considered above, the procedure of the subtraction of the projections obtained at different spectral compositions of radiation ensures an increased contrast of the image

displayed on the screen and emphasizes the boundaries between the structural details.

(2) An efficient scheme for subtracting projections in the energy range ~10 keV can be implemented on the base of a standard X-ray tube with selective filters.

(3) An enhancement of the difference-image contrast is explained by the matching of the range of the signal variation over the difference-image field to the dynamic range of screen-brightness gradations perceived by the observer.

(4) Optimal conditions for obtaining difference images can be achieved using the proposed recording schemes with an X-ray spectrum controlled by semitransparent monochromators. These schemes ensure (a) the complete coincidence of elements of the images in different spectral ranges for the subsequent color coding and (b) the recording of dynamic difference images in vivo without motion artifacts.

ACKNOWLEDGMENTS

We are grateful to V.I. Tsekhosh for the data-scale optimization program in the conversion of 12-bit images and N.Yu. Narimanova for preparing contrast solutions and preparations.

This work was supported by the American Civil Research and Development Foundation, grant no. RP-22105.

REFERENCES

1. Lindenbraten, L.D. and Naumov, L.B., *Meditsinskaya rentgenologiya* (Medical Rontgenology), Moscow: Meditsyna, 1984.
2. Ishchenko, B.I., Bisenkov, L.N., and Tyurin, I.E., *Luchevaya diagnostika dlya torakal'nykh khirurgov* (Radiation Diagnostics for Thoracal Surgeons), St-Petersburg: DEAN, 2001, p. 346.
3. *Rukovodstvo po angiografii* (Handbook on Angiography), Rabkin, I.Kh., Ed., Moscow: Meditsyna, 1977, p. 288.
4. Sergeev, P.V., Sviridov, N.K., and Shimanovskii, N.L., *Rentgenokontrastnye veshchestva* (X-ray Contrast Substances), Moscow: Meditsyna, 1980, p. 240.
5. Bykov, R.E., Kozlovskii, E.B., and Mazurov, A.I., *Tekhnicheskie sredstva meditsinskoi introskopii* (Medical Introscopy Equipment), Leonov, B.I., Ed., Moscow: Meditsyna, 1989, pp. 103–143.
6. Kondratyev, V.I., Kulipanov, G.N., Kuzin, M.V., *et al.*, *Medical Applications of Synchrotron Radiation,* Ando, M. and Uyama, C., Eds., Tokyo: Springer, 1998, pp. 29–32.
7. Dill, T., Ventura, R., and Dix, W.-R., *et al, Medical Applications of Synchrotron Radiation*, Ando, M. and Uyama, C., Eds., Tokyo: Springer, 1998, pp. 22–28.
8. Bessonov, E.G., Vinogradov, A.V., and Tur'yanskii, A.G., *Prib. Tekh. Eksp.*, 2002, no. 5, p. 142.
9. Tur'yanskii, A.G. and Pirshin, I.V., *Prib. Tekh. Eksp.*, 1998, no. 5, p. 118.
10. Tur'yanskii, A.G., Vinogradov, A.V., and Pirshin, I.V., *Prib. Tekh. Eksp.*, 1999, no. 1, p. 105.
11. Nesterets, Ya.I., Punegov, V.I., Pirshin, I.V., *et al.*, *Phys. Status Solidi A,* 2000, vol. 179, p. 311.
12. Touryanski, A.G., Vinogradov, A.V., and Pirshin, I.V., *Nucl. Instrum. Methods Phys. Res A.*, 2000, vol. 448, p. 184.
13. Tur'yanskii, A.G. and Pirshin, I.V., *Prib. Tekh. Eksp.*, 2000, no. 4, p. 117.
14. James., R.W., *The Optical Principles of the Diffraction of X-Rays*, London, 1950.
15. Iveronova, V.I. and Revkevich, G.P., *Teoriya rasseyaniya rentgenovskikh luchei* (Theory of X-Ray Scattering), Moscow: Mosk. Gos. Univ., 1978.
16. Lerner, E.J., *Laser Focus World*, 2001, no. 12 (December), p. 109.
17. Smith, R.F. and Key, M.H., *Proc. SPIE,* 2001, vol. 4500, p. 24.
18. Schoenlein, R.W., Leemans, W.P., Chin, A.H., *et al.*, *Science*, 1996, vol. 274, p. 236.
19. *Rentgenotekhnika. Spravochnik* (X-Ray Engineering. Handbook), Klyuev, V.V., Ed., Moscow: Mashinostroenie, 1980, vol. 1.
20. Kumakhov, M.A. and Komarov, F.F., *Phys. Rep.*, 1990, vol. 191, no. 5, p. 289.
21. Kumakhov, M., *X-ray Spectrom.*, 2000, vol. 29, p. 343.
22. Novitskii, P.V. and Zograf, I.A., *Otsenka pogreshnosti rezul'tatov izmerenii* (Estimation of Errors in Experimental Results) Leningrad: Energoatomizdat, 1985.
23. Rumyantsev, S.V., Shtan', A.S., and Gol'tsev, V.A., *Spravochnik po nerazrushayushchim metodam kontrolya* (A Handbook of Nondestructive Testing), Moscow: Energoatomizdat, 1982.
24. *Elektronika. Entsiklopedicheskii slovar'* (Electronics. Encyclopaedia), Moscow: Sov. Entsiklopediya, 1991.
25. Gurvich, A.M., *Fizicheskie osnovy radiatsionnogo kontrolya i diagnostiki* (Physical Foundations of Radiation Control and Diagnostics), Moscow: Energoatomizdat, 1989.
26. Blinov, N.N., Bykov, R.E., Leonov, B.I., *et al.*, in *Tekhnicheskie sredstva meditsinskoi introskopii* (Medical Introscopy Equipment), Moscow: Meditsyna, 1989, pp. 6–48.
27. Halmshaw, R., *Research Techniques in Nondestructive Testing*, Sharpe, R.S., Ed., London: Academic, 1970.
28. Krasil'nikov, N.N., *Teoriya peredachi i vospriyatiya izobrazhenii* (Theory of Transmission and Perception of Images), Moscow: Radio i Svyaz', 1986, p. 248.
29. *Bildgebende Systeme Fur Medizinishe Diagnostik,* Berlin: Siemens Aktiongesellschaft, 1980.
30. Taits, A.M. and Taits, A.A., *Adobe® Photoshop 5.5. Samouchitel'* (Adobe(r) Photoshop 5.5. Self-Taught), St. Petersburg: BKhV-Sankt-Peterburg, 2000, p. 544.
31. *Whole Body CT Scanner TCT-600HQ*, Toshiba Corporation, Brochure.

32. Blokhin, M.A. and Shveitser, I.G., *Rentgenospektral'nyi spravochnik* (Handbook on X-ray Spectra), Moscow: Nauka, 1982.
33. Dyson, N.A., *X-Rays in Atomic and Nuclear Physics*, Longman, 1973.
34. Tur'yanskii, A.G., Pirshin, I.V., Khmel'nitskii, R.A., and Gippius, A.A., *Fiz. Tverd. Tela*, 2001, vol. 43, no. 4, p. 619.
35. Protopopov, V.V. and Kalnov, V.A., *Opt. Commun.*, 2000, vol. 184, p. 1.
36. Momose, A., Takeda, T., and Itai, Yu., *Radiology*, 2000, vol. 217, p. 593.
37. Momose, A., US Patent 5930325, 1999.
38. Arfelli, F., Bonvicini, V., Bravin, A., *et al.*, *Radilogy*, 2000, vol. 215, p. 286.
39. Ingal, V.N. and Beliavskaya, E.A., *J. Phys. D: Appl. Phys.*, 1995, vol. 28, p. 2314.
40. Ingal, V.N., Belyavskaya, E.A., and Efanov, V.P., US Patent 5579363, 1996.
41. Bushuev, V.A. and Sergeev, A.A., *Pis'ma Zh. Tekh. Fiz.*, 1998, vol. 24, no. 21, p. 55.
42. Snigirev, A., Kohn, V., Snigireva, I., and Lengeier, B., *Nature* (London), 1996, vol. 384, p. 49.